EUROPEAN JOURNAL OF COMPUTATIONAL MECHANICS
2018, VOL. 27, NOS. 5–6, 479–507
https://doi.org/10.1080/17797179.2018.1550961

Taylor & Francis
Taylor & Francis Group

A simple vortex approach to complex two-wing unsteady flapping problems in 2D applied to insect flight study

Mitsunori Denda, Roberta Shapiro and Justin Wong

Mechanical and Aerospace Engineering Department, Rutgers University, Piscataway, NJ, USA

ABSTRACT
The secrets of the flapping of insects with two pairs of wings, primarily dragonflies, have been revealed experimentally and numerically. Although there exist many excellent experimental studies, numerical study is limited due to the highly demanding nature of the numerical approach to the unsteady flapping problems. Recently, we have developed a vortex-based method for the single-wing flapping problems in 2D. The simplicity and the accuracy of the method developed have encouraged us to extend the method to problems with two pairs of wings; the outcome is reported in this paper. We consider the species with a long wing span for which the flow field in the span direction is constant and treated as 2D.

ARTICLE HISTORY
Received 29 November 2017
Accepted 19 November 2018

KEYWORDS
Vortex method; two-wing (two pairs of wings) flapping; 2D unsteady flow; insect flight

1. Introduction

While birds and flying mammals use their wing muscles and bones to actively morph the wing contour, insects use passive mechanisms that rely on the wing structural design to achieve the optimal wing shape. The absence of an additional control mechanism in insect wings makes them light and suited for adaptation in the design of extremely lightweight micro-areal vehicles.

Another distinction between birds and insects is the number of wings; birds have two wings while flying insects have four. According to Wigglesworth (1972), in Orthoptera (grasshopper, cricket, katydid and locust), Neuroptera (lacewing, mantidfly and antlion), Isoptera (termite) and Odonata (dragonfly and damselfly), the fore and hind-wings move independently. Wigglesworth compares the flight of Orthoptera and lower Neuroptera to that of Odonata (dragonflies). While the upstroke and downstroke of the fore-wings for the former group of insects are in advance of the hind-wings, dragonflies reverse the order of the wing beat to 'meet the oncoming air before it is troubled by

CONTACT Mitsunori Denda ✉ denda@rutgers.edu

The underlying research materials for this article can be accessed at **Movie 1**: https://youtu.be/oXsq1sUou74; **Movie 2**: https://youtu.be/OEWHxwPBHm8; **Movie 3**: https://youtu.be/pGpsvsDdqUg; **Movie 4**: https://youtu.be/qDZzLwfUExg; **Movie 5**: https://youtu.be/8a7MfqqFPmc

the passage of the fore-wings'. In Hymenoptera (bee), Lepidoptera (butterfly and moth) and Hemiptera (true bug), 'fore and hind-wings are united by various mechanisms to make a functional unit' to avoid 'the disadvantage of the second pair of wings working in a region of turbulence produced by the first pair'.

Although there exist many excellent experimental studies (Rival, Widmann, & Tropea, 2012; Thomas, Taylor, Srygley, Nudds, & Bomphery, 2004), there are few numerical studies of two pairs of wings, including the blade element method (Azuma & Watanabe, 1988), the upwind differencing scheme (Wang & Sun, 2005) and the immersed boundary method (Wang & Russell, 2007), due to the highly demanding nature of the numerical approach to the unsteady flapping problems. So far, dragonflies have been studied almost exclusively, but it will be instructive to shed light to the flight of other insects.

The primary goal of this paper is to develop a simple but accurate numerical method for analysing the unsteady fluid flow generated by the pairs of fore and hind-wings moving independently. We consider insects with a long wing span for which the flow field in the span direction is constant and then reduce the problem to 2D, in which the original fore and hind pairs (four wings) in 3D are modelled by two wings in 2D, represented by one fore-wing and one hind-wing. The vortex-based method used in this paper has been verified as simple but highly reliable for the study of unsteady flapping aerodynamics for one pair of wings (modelled by a single-wing in 2D) (Denda, Jujjavarapu, & Jones, 2016). The flow observed in the flapping flight has a low Reynolds number for which the viscous effects are important and the wake region is turbulent. The proposed vortex approach that models the viscous boundary layers on the wings and the turbulent wake region surrounding the wings is capable of modelling the realistic viscous and turbulent flows. The method is applicable regardless of the Reynolds number; for large Reynolds numbers, the number of vortices increases and the problem of turbulence is reduced to the many-wake-vortices problem in the inviscid fluid. In this paper, the method, originally developed for the single pair of wings, is extended to the two pairs of wings in 2D; for simplicity, the former is called the 'single-wing problem' and the latter the 'two-wing problem.'

2. Coordinate systems

For insects with a long wing span, the flow remains approximately constant in the span direction. This justifies the two-dimensional (2D) modelling of wing motion. This paper considers such a class of 2D wing motions, for which the flow field does not change in the out-of-plane direction. Two infinitely long wings (in the span direction) are represented by their intersections with the two-dimensional plane as two thin chords of wings. The wings are assumed rigid.

The position of each wing is described locally by the wing-fixed system $O-\xi\eta$ and globally by the space-fixed system $\tilde{O}-\tilde{\xi}\tilde{\eta}$ as shown in Figure 1. Each wing undergoes two translational (lunge and heave) and one rotational (pitch) motions (described below). We introduce a third coordinate system for each wing, with its origin, $\hat{O}-\hat{\xi}\hat{\eta}$, placed at the centre of rotation of the wing, which is located at

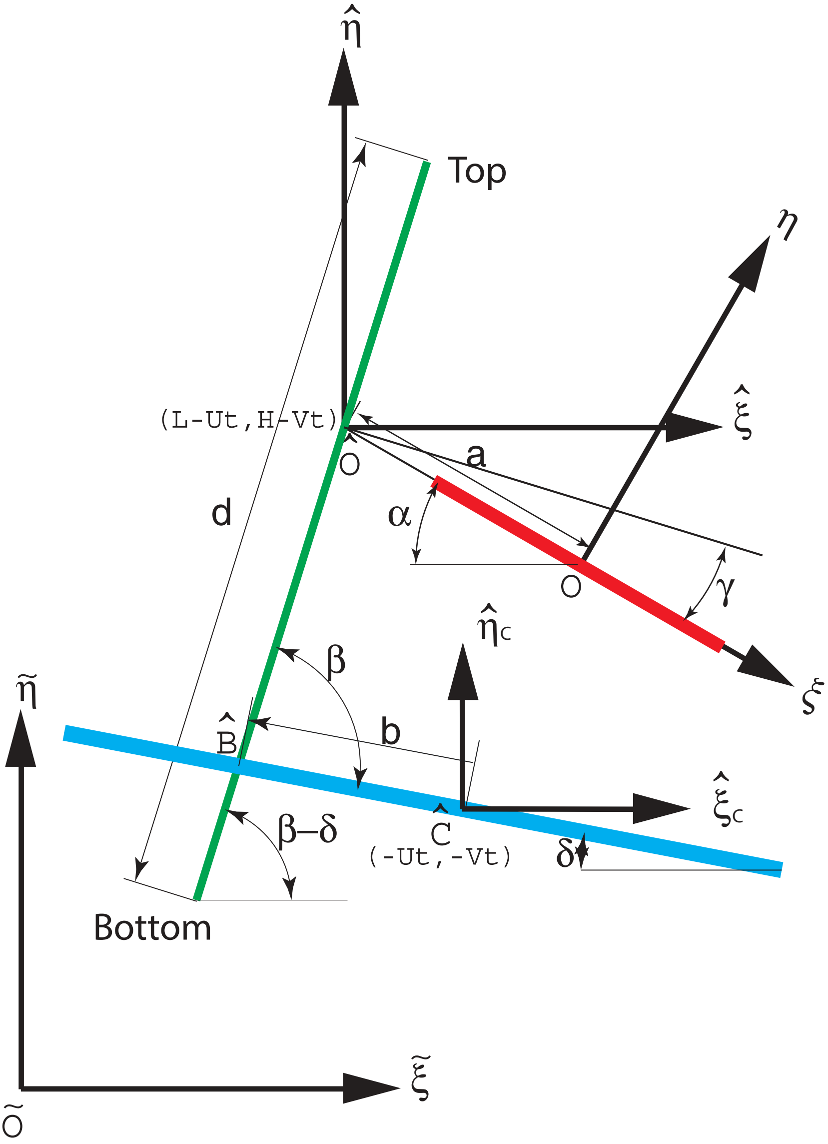

Figure 1. Space-fixed ($\tilde{O}-\tilde{\xi}\tilde{\eta}$), wing-fixed ($O-\xi\eta$) and wing-translating ($\hat{O}-\hat{\xi}\hat{\eta}$) coordinate systems along with the body-fixed system $\hat{C}-x_C z_C$ for a single wing.

a distance a (the rotational offset) along the negative ξ axis. The axes, $\hat{\xi}$ and $\hat{\eta}$, of the last system are parallel to the global $\tilde{\xi}$ and $\tilde{\eta}$ axes, respectively. While the wing-fixed system rotates and translates with the wing, the system $\hat{O}-\hat{\xi}\hat{\eta}$ only translates and is called the wing-translating system.

For each wing, the trajectory of the translational wing motion, or the trace of the origin $\hat{O}$ of the wing-translating system, is described by a line called the stroke line. We introduce the body-fixed system $\hat{C}-\hat{\xi}_C\hat{\eta}_C$, whose origin is located at the mass centre $\hat{C}$ with vertical and horizontal axes. In addition, we introduce a straight axis (the body axis) aligned with the body of the insect. The angle of the body axis and the stroke line angle with respect to the body axis are given by δ and β, respectively, such that the stroke line angle in the space-fixed system is $\beta-\delta$. Figure 2 shows two sets of wing-fixed and wing-translating systems along with the common space-fixed system $\tilde{O}-\tilde{\xi}\tilde{\eta}$ and the body-fixed system $\hat{C}-\hat{\xi}_C\hat{\eta}_C$. Notice that subscripts F and H in Figure 2 indicate quantities for fore and hind-wings. See further details in Appendix A.

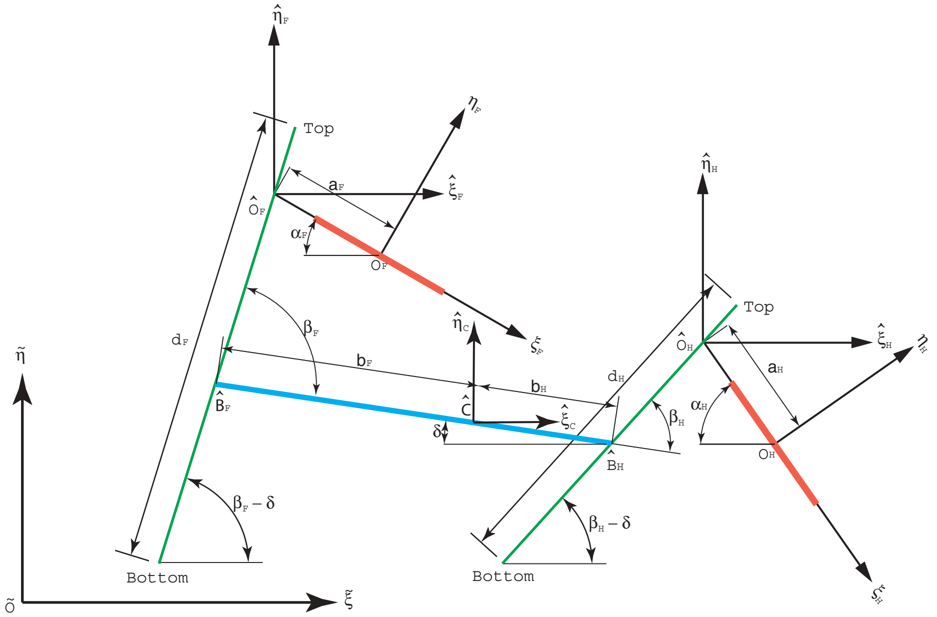

Figure 2. Space-fixed ($\tilde{O}-\tilde{\xi}\tilde{\eta}$), wing-fixed ($O_F-\xi_F\eta_F$, $O_H-\xi_H\eta_H$), wing-translating ($\hat{O}_F-\hat{\xi}_F\hat{\eta}_F$, $\hat{O}_H-\hat{\xi}_H\hat{\eta}_H$), stroke line ($\hat{F}-x_Fz_F$, $\hat{H}-x_Hz_H$) and body ($\hat{C}-x_Cz_C$) coordinate systems. Subscripts F and H indicate the fore and hind-wings, respectively.

3. 2D motion of insect wings

3.1. Motion of the single wing

3.1.1. Wing motion

The motion of the individual insect wing in three-dimensions consists of three rotational components (roll, pitch and yaw) and three translational components. In 2D, the roll is recast as a translational motion consisting of the heave (up and down) and lunge (forward and back) components. The pitch remains as the same in 3D and the yaw does not exist. Superimposed upon these rotational contributions is the translational motion of the insect in the negative space-fixed coordinate direction.

While the rolling of a finite length insect wing in 3D is described by the rotation around the body axis, it is represented in 2D by a translational motion (horizontal or lunge, L, and vertical or heave, H, components) of an infinitely long wing along the stroke line. Additionally, the wing rotates about the wing span axis to produce the pitch measured by the angle γ (positive clockwise). The forward pitch (downstroke direction with $\gamma < 0$) and backward pitch (upstroke direction with $\gamma > 0$) are called the pronation and supination, respectively.

Consider a 3D rolling motion of an insect wing of the span length $\mathcal{L} = 2l$ over a stroke plane, which is the trajectory of the centre line of the wing span. Let the upper and lower extents of the rolling motion be given by the upper and lower stroke angles, ϕ_T and ϕ_B, as shown in Figure 3. These three quantities, taken from the actual insect flight motions, are used to specify the extent of the stroke line by the trajectory of the midpoint, l, of the span into the 2D plane. Since the linear distance travelled by points along the wing span increases from 0, at the base, to the maximum, at the wing tip, its projection is taken at the midpoint, giving the average. The time variation of the lunge and heave is expressed using the sinusoidal function.

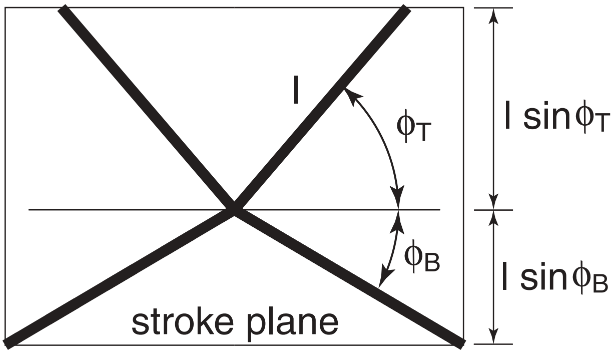

Figure 3. The stroke plane view of the topmost (ϕ_T) and bottommost (ϕ_B) positions of the wing midpoint. Half wing spans on the left and right sides are shown, each at the extreme positions.

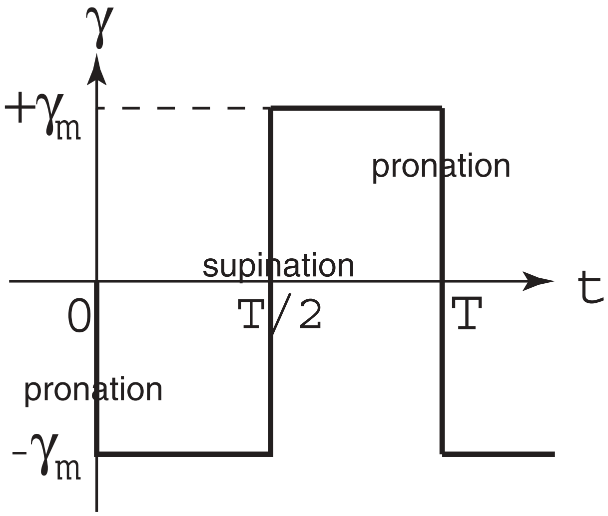

Figure 4. Perfect pronation and supination.

The pitch motion occurs as a sudden rotation, described by the step function, of the wing at the extremes of each stroke (symmetric pitch), as shown in Figure 4. It consists of the pronation in the downward direction and the supination in the upward direction at the top and the bottom of the stroke, respectively. The pitch motions that occur before and after reaching the top or bottom are called advanced and delayed pitches, respectively. Most insects do not have the capability to pitch instantaneously and the rotation is smoothed out throughout the stroke. A smooth step function, as shown in Figure 5, is used.

The effect of the insect flight speed, (U, V), is incorporated by moving the wing itself in the direction opposite to the air velocity under zero ambient velocity. The non-zero ambient velocity can be superimposed over this. For a constant air velocity, the total translational motion of the wing is obtained by superimposing the contributions, L (lunge) and H (heave), from the flapping motion and the air velocity to give $(L - Ut, H - Vt)$, where t is the time.

All of the variables describing wing position are displayed in Figure 1. Here, $(L - Ut, H - Vt)$ gives the coordinates of the wing-translating system origin $\hat{O}$, α gives the slope of the ξ-axis of the wing-fixed system, and a is the distance between the origins of the wing-fixed and wing-translating systems. Notice that the coordinates of the body-fixed system origin $\hat{C}$ are given by $(-Ut, -Vt)$. Additionally, the slope of the body axis is δ and the location of the origin, $\hat{B}$, of the stroke line coordinate system from the body centre $\hat{C}$ is given by b. The details of the individual wing motion are given in Appendix B.

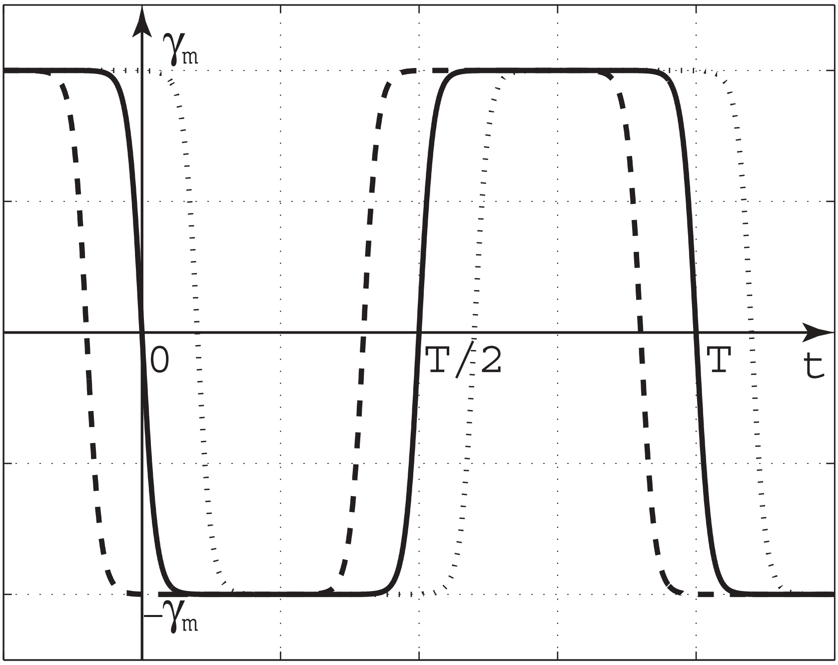

Figure 5. Smoothed pitch motion with symmetric (solid), advanced (dashed) and delayed (dotted) pitch.

3.1.2. Wing velocity

The origin of the wing-translating system moves with velocity $(\dot{L} - U, \dot{H} - V)$, while the origin of the wing-fixed system moves with combined translational $(\dot{L} - U, \dot{H} - V)$ and rotational $(\dot{\alpha})$ velocities as shown in Figure 6. The origin $\hat{O}$ of the wing-translating system is the centre of rotation. The velocity of an arbitrary point $P = (\xi, \eta)$ on the wing is given, in terms of these wing velocity parameters, by

$$V_{\tilde{\xi}} = \dot{L} - U + \dot{\alpha}(\eta\cos(\alpha) - (a + \xi)\sin(\alpha))\,\text{and} \tag{1}$$

$$V_{\tilde{\eta}} = \dot{H} - V - \dot{\alpha}((a + \xi)\cos(\alpha) + \eta\sin(\alpha))$$

in the space-fixed coordinate system (Denda et al., 2016), where α is the attack angle of the wing.

We consider a straight wing. The complex-valued unit normal vector is given by

$$\tilde{n} = n_{\tilde{\xi}} + in_{\tilde{\eta}} = ie^{-i\alpha} \tag{2}$$

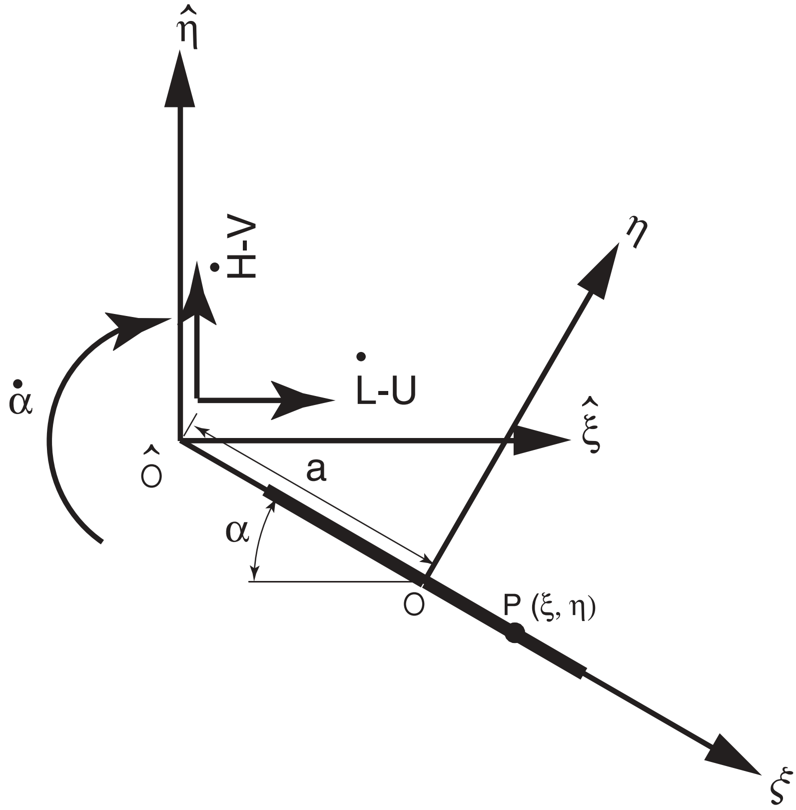

Figure 6. Translational and rotational velocities of the wing-translating and wing-fixed coordinate systems.

in the space-fixed system, where i is the imaginary number (Denda et al., 2016). The normal velocity of the wing is given, from Equations (1) and (2), by

$$V^{\tilde{n}} = \Re(\bar{V}_{\tilde{\zeta}} \tilde{n}) = V_{\tilde{\xi}} n_{\tilde{\xi}} + V_{\tilde{\eta}} n_{\tilde{\eta}}, \tag{3}$$

where $\Re()$ is the real part of a complex variable. Although we are assuming the straight wing in this paper, the camber of the wing can readily be introduced by replacing i in Equation (2) by the complex valued unit normal to the curved wing.

3.2. Motion of two wings

The motion of the second wing is described exactly in the same manner as the first wing mentioned above. When two wings are present, parameters for each wing are distinguished from those of the other wing by using the subscripts F and H for the fore and hind-wings, as seen in Figure 2.

4. Vortex equations

4.1. Single vortex

The vortices used in this paper are conveniently described in terms of complex variables (Sears, 2011). Consider a line vortex with the circulation Γ (positive counter-clockwise) located at $\tilde{\zeta}_0 = \tilde{\xi}_0 + i\tilde{\eta}_0$. Its complex potential function is given by

$$\omega(\tilde{\zeta}) = -\frac{i\Gamma}{2\pi}\log(\tilde{\zeta} - \tilde{\zeta}_0), \tag{4}$$

where $\tilde{\zeta} = \tilde{\xi} + i\tilde{\eta}$ and $\tilde{\zeta}_0$ are complex position vectors in the space-fixed system. The corresponding conjugate complex velocity is given by

$$\overline{v(\tilde{\zeta})} = \frac{d\omega}{d\tilde{\zeta}} = -\frac{i\Gamma}{2\pi}\frac{1}{\tilde{\zeta} - \tilde{\zeta}_0}, \tag{5}$$

where $v(\tilde{\zeta}) = v_{\tilde{\xi}} + iv_{\tilde{\eta}}$ and an overbar $\overline{(\,)}$ indicates the complex conjugate.

To avoid an excessively high value of the velocity when it is evaluated in the neighbourhood of the source point, we introduce the vortex core model (Denda et al., 2016) for which Equation (5) is used outside the core radius only. Within the core radius, the velocity changes linearly from 0 to a value, given by Equation (5), on the radius of the core.

4.2. Discretisation of the wing

For each wing, introduce m vortices Γ_j at $\tilde{\zeta}_{0j}$ $(j = 1, 2..., m)$, and $m - 1$ collocation points $\tilde{\zeta}_i$ $(i = 1, 2..., m - 1)$ on the wing. The collocation points are placed at the midpoints of vortex points. The number of vortices for two wings, m_F and m_H, may differ (notice the subscript convention, F and H, used for the two-wing system). We place vortices at the leading (LE) and trailing (TE) edges and in between. The spacing of the vortex points could be equidistant at the middle and gradually narrowed towards the two end points, which are mathematically known singular points. The details are given by Denda et al. (2016).

4.3. Influence coefficients

For the two-wing system, there are two types of influence coefficients between vortices located on the two wings: self and cross-influence functions. The complex conjugate velocity at the fore-wing collocation point $\tilde{\zeta}_{F_i}$ due to a fore-wing vortex Γ_{F_j} at $\tilde{\zeta}_{F_{0j}}$ is given by

$$\bar{v}_{F_iF_j} = -\frac{i\Gamma_{F_j}}{2\pi}\frac{1}{\tilde{\zeta}_{F_i}-\tilde{\zeta}_{F_{0j}}}. \tag{6}$$

The normal component of this velocity at the fore-wing collocation point is given, from Equation (3), by

$$v^{\tilde{n}_F}_{F_iF_j} = \Re(\bar{v}_{F_iF_j}\tilde{n}_{F_i}) = \frac{\Gamma_{F_j}}{2\pi}\Im\left(\frac{\tilde{n}_{F_i}}{\tilde{\zeta}_{F_i}-\tilde{\zeta}_{F_{0j}}}\right)\equiv V^{\tilde{n}_F}_{F_iF_j}\Gamma_{F_j}, \tag{7}$$

where $\tilde{n}_{F_i}$ is given by Equation (2) at the fore-wing collocation point, $\Im$ is the imaginary part of a complex variable, and

$$V^{\tilde{n}_F}_{F_iF_j} = \frac{1}{2\pi}\Im\left(\frac{\tilde{n}_{F_i}}{\tilde{\zeta}_{F_i}-\tilde{\zeta}_{F_{0j}}}\right) \tag{8}$$

is the self-influence coefficient for the fore-wing. Another self-influence function for the hind-wing, $V^{\tilde{n}_H}_{H_iH_j}$, is obtained from Equation (8) by replacing the subscript F by H. Two more cross-influence functions that describe the interaction between the fore and hind-wings, $V^{\tilde{n}_F}_{F_iH_j}$ and $V^{\tilde{n}_H}_{H_iF_j}$, are obtained similarly. For example, the former is the cross-influence function for the normal velocity on a fore-wing collocation point F_i due to a hind-wing vortex Γ_{H_j}.

5. System of equations for discrete vortices on two wings

5.1. Contribution from the bound vortices on two wings

In this subsection, we only consider bound vortices on the two wings; the effect of the wake vortices is added in the next subsection. At the fore-wing collocation point $\tilde{\zeta}_{Fi}$, calculate the normal velocity component contributions from the discrete bound vortices of the fore and hind-wings to get

$$v^{\tilde{n}_F}_{F_i} = \sum_{F_j=1}^{m_F} V^{\tilde{n}_F}_{F_iF_j}\Gamma_{F_j} + \sum_{H_j=1}^{m_H} V^{\tilde{n}_F}_{F_iH_j}\Gamma_{H_j}, \tag{9}$$

where $V^{\tilde{n}_F}_{F_iF_j}$ is given by Equation (8) and $V^{\tilde{n}_F}_{F_iH_j}$ is one of cross-influence coefficients between two wings. The non-penetration condition requires that this normal velocity must be equal to the normal velocity of the fore-wing, $V^{\tilde{n}_F}_{F_i}$, at each collocation point,

$$\sum_{F_j=1}^{m_F} V^{\tilde{n}_F}_{F_iF_j}\Gamma_{F_j} + \sum_{H_j=1}^{m_H} V^{\tilde{n}_F}_{F_iH_j}\Gamma_{H_j} = V^{\tilde{n}_F}_{F_i}, \tag{10}$$

for collocation points $F_i = 1, 2, ..., m_F - 1$. An additional equation, required to match the number of m_F unknowns, Γ_{F_i}, for the fore-wing is given by the conservation of the fore-wing vortices,

$$\sum_{F_j=1}^{m_F} \Gamma_{F_j} = 0. \tag{11}$$

Similarly, the system of equations for the hind-wing is obtained by swapping the subscripts F and H in Equations (10) and (11) with the result

$$\sum_{F_j=1}^{m_F} V_{H_iF_j}^{\tilde{n}_H} \Gamma_{F_j} + \sum_{H_j=1}^{m_H} V_{H_iH_j}^{\tilde{n}_H} \Gamma_{Hj} = V_{H_i}^{\tilde{n}_H}, \tag{12}$$

for collocation points $H_i = 1, 2, ..., m_H - 1$ and the hind-wing vortex conservation equation

$$\sum_{H_j=1}^{m_H} \Gamma_{H_j} = 0. \tag{13}$$

Notice that the vortex conservation condition is applied for each wing independently in order to provide two additional equations, thus securing the sufficient number of equations and matching the total number of bound vortices, $m_F + m_H$.

5.2. Contribution from the wake vortices

At each time step, a pair of fore-wing vortices, from the leading ($F_j = M_F$) and trailing ($F_j = 1$) edges, are shed from the fore-wing. This results in, during the p th time period, $2(p - 1)$ fore-wing wake vortices,

$$\Gamma_{F_1}^{[k]} \text{ and } \Gamma_{F_m}^{[k]} \tag{14}$$

located at

$${}^{[p]}\tilde{\zeta}_{F_1}^{[k]} \text{ and } {}^{[p]}\tilde{\zeta}_{F_m}^{[k]}, \tag{15}$$

where the pre-superscript ${}^{[p]}()$ indicates the current step $[p]$ and the post-superscript $()^{[k]}$ $(k = 1, 2, ..., p - 1)$ indicates the originating time step. Since the values of Γ_F's remain constant once the vortices are shed into the flow, they do not have the pre-superscript. Following the procedure used in the previous subsection for the calculation of bound vortex-induced velocity, we can obtain (Denda et al., 2016) the normal components, ${}^{[p]}v_{F_iF_p}^{\tilde{n}_F}$ and ${}^{[p]}v_{H_iF_p}^{\tilde{n}_H}$, of fore-wing wake-induced velocity at the fore and hind-wing collocation points $\tilde{\zeta}_{F_i}$ and $\tilde{\zeta}_{H_i}$, respectively.

The effects of the wake vortices shed from the hind-wing can be treated similarly to obtain the normal components, ${}^{[p]}v^{\tilde{n}_F}_{F_iH_p}$ and ${}^{[p]}v^{\tilde{n}_H}_{H_iH_p}$, of hind-wing wake-induced velocity at the fore and hind-wing collocation points $\tilde{\zeta}_{F_i}$ and $\tilde{\zeta}_{H_i}$, respectively.

Equations (10) and (12) are now augmented with the contributions from the wake vortices, yielding

$$\sum_{F_j=1}^{m_F} V^{\tilde{n}_F}_{F_iF_j}\Gamma_{F_j} + \sum_{H_j=1}^{m_H} V^{\tilde{n}_F}_{F_iH_j}\Gamma_{H_j} + {}^{[p]}v^{\tilde{n}_F}_{F_iF_p} + {}^{[p]}v^{\tilde{n}_F}_{F_iH_p} = V^{\tilde{n}_F}_{F_i} \tag{16}$$

and

$$\sum_{F_j=1}^{m_F} V^{\tilde{n}_H}_{H_iF_j}\Gamma_{F_j} + \sum_{H_j=1}^{m_H} V^{\tilde{n}_H}_{H_iH_j}\Gamma_{H_j} + {}^{[p]}v^{\tilde{n}_H}_{H_iF_p} + {}^{[p]}v^{\tilde{n}_H}_{H_iH_p} = V^{\tilde{n}_H}_{H_i}. \tag{17}$$

Notice that for the first step, the wake is absent, and so are the augmented wake vortex contributions in Equations (16) and (17).

6. Convection of wake vortices, shedding of bound edge vortices and the Kutta condition

In our proposed method, the Kutta condition is not enforced at the LE and TE of two wings (Belotserkovsky, Kotovskii, Nisht, & Fedorov, 1993; Belotserkovsky& Lifanov, 2003; Denda et al., 2016). Instead the bound vortices at these points are shed regularly at each time step. Right after shedding, the two edges of each wing lose vortices to effectively satisfy the Kutta condition momentarily until the new bound vortices are built up in the next time step. All wake vortices are convected using the velocity calculated at the wake vortices. The velocity contributions come from the bound and wake vortices of the two wings.

7. Time marching solution procedure

In the time marching solution procedure, we prescribe the wing position and velocity of two wings for each time step. Then, determine the magnitudes of the bound vortices using the non-penetration condition, Equations (16) and (17), and vortex conservation equations, Equations (11) and (13), for two wings. Next, calculate the induced velocity at the TE and LE of two wings and wake vortex sites. Finally, shed the edge vortices and convect the wake vortices. We repeat the whole process for the subsequent time steps. For a detailed description of the time marching solution procedure for the single wing, see Denda et al. (2016), which is essentially the same for two-wing case in this paper.

8. Impulses and force/moment

8.1. *Space-fixed system*

Denda et al. (2016) have shown that the linear and angular impulses of a line vortex located at $\tilde{\zeta} = \tilde{\xi} + i\tilde{\eta}$ with the circulation Γ are given by

$$-\,i\rho\Gamma\tilde{\zeta} \tag{18}$$

and

$$-\frac{1}{2}\rho\Gamma|\tilde{\zeta}|^2, \tag{19}$$

where Γ is a signed circulation with positive counter-clockwise orientation. The time derivatives of the linear and angular impulses will provide the force and moment exerted by the vortex onto the air. The force and moment acting on the two wings are obtained by reversing the signs of those obtained for the air. Notice that these are the resultants on the two wings and the current approach cannot identify those acting on the individual wing.

8.2. *Wing-translating system*

The linear and angular impulses must be calculated in the space-fixed system. However, the angular momentum about the origin of the space-fixed system is inapplicable in practical applications. Rather, it should be calculated about the origin $\hat{C}$ of the body-fixed system (see Figure 2). The problem, however, is that its origin is moving. To resolve this issue, we introduce another space-fixed system that has the same origin as the body-fixed system and calculate the angular impulse in this coordinate system. Although this system needs to be updated as the body-fixed system moves, each one of them in time history is a space-fixed system and is the legitimate system for the calculation of the impulses.

Consider, first, the original space-fixed system $\tilde{O} - \tilde{\xi}\tilde{\eta}$ and the body-fixed system $\hat{C} - \hat{\xi}_c\hat{\eta}_c$. The transformation between the two systems is given by

$$\tilde{\zeta} = r + \hat{\zeta}_C, \tag{20}$$

where $\hat{\zeta}_C = \hat{\xi}_C + i\hat{\eta}_C$ and $r = -Ut - iVt$. Substitute this relation into Equations (18) and (19) and simplify to obtain

$$\tilde{\mathcal{I}} = \hat{\mathcal{I}}, \tilde{\mathcal{I}}_A = \hat{\mathcal{I}}_A + \Im(\bar{r}\hat{\mathcal{I}}), \tag{21}$$

where

$$\hat{\mathcal{I}} = -i\rho\Gamma\hat{\zeta} \text{ and } \hat{\mathcal{I}}_A = -\frac{1}{2}\rho\Gamma|\hat{\zeta}|^2. \tag{22}$$

Now take the time derivative in Equation (21) to get the force and moment,

$$\tilde{\mathcal{F}} = \dot{\tilde{\mathcal{I}}} = \dot{\hat{\mathcal{I}}},^{\sim} = \dot{\hat{\mathcal{I}}}_A = \dot{\hat{\mathcal{I}}}_A + \Im(\dot{\bar{r}}\hat{\mathcal{I}}) + \Im(\bar{r}\dot{\hat{\mathcal{I}}}). \tag{23}$$

At this point, we switch from the original space-fixed system to the space-fixed system that is placed on top of the body-fixed system, for which $r = 0$, giving the updated relations

$$\tilde{\mathcal{F}} = \dot{\tilde{\mathcal{I}}} = \dot{\hat{\mathcal{I}}},^{\sim} = \dot{\tilde{\mathcal{I}}}_A = \dot{\hat{\mathcal{I}}}_A + \Im(\dot{\bar{r}}\hat{\mathcal{I}}), \tag{24}$$

where $\dot{\bar{r}} = -U + iV$ is the conjugate complex velocity of the coordinate origin $\hat{C}$ of the body-fixed system due to the wing translational motion. Finally, the force and moment acting on the two wings are obtained by reversing the signs.

In 2D, the force and moment are calculated per unit depth. Consider an insect with the span length $\mathcal{L} = 2l$. In 3D, the wing undergoes a radial flapping motion about the wing base. In the 2D adaptation of this flapping motion, we determine its stroke line length d by projecting the 3D flapping motion of the midpoint at l, rather than the wing tip at $2l$, in order to represent the average stroke line length of the 3D flapping wing.

Note that the programme inputs the half-span length l and obtains the force and moment per unit span length. The total force and moment are calculated by multiplying the span length $\mathcal{L} = 2l$. Counting wings on the right and left, we further double the total force and moment.

9. Evaluation of numerical performance

The vortex method used in this paper is essentially the influence function method, similar to the BEM (boundary element method), in comparison to the domain methods such as the FVM (finite volume method) and FEM (finite element method). The domain method, in the extension from the single to multiple-wing analysis, must be carefully re-examined. The strategies working for the single-wing analysis may not work for multiple-wing case any more. For example, when two wings get closer, the mesh between them must be refined accordingly, which is not required for the single-wing analysis.

The influence function method depends on the concept of closeness between two points in the field or the distance between the source and observation points. Because of this, the strategies developed for the single-wing analysis remain valid for multiple-wing case regardless of the relative position of the multiple wings. In other words, the strategies dealing with the closeness of multiple-wing case are already built in the single-wing analysis. If they work for the single-wing analysis, then they also work for multiple-wing case. This fact plays a key role in extending the vortex method from the single to the multiple-wing case. There is no question that the verification must be performed for the single-wing case against the established method such as the FVM as in Denda et al. (2016). After this, however, there is not need to verify the vortex method against the multiple-wing case.

In the following, we review the strategies developed to deal with the closeness between two points in the single-wing analysis. Denda et al. (2016) have evaluated the numerical performance of the proposed vortex method for a single-wing problem in 2D. First, the closeness between two bound vortices is explored. The spacial resolution is determined by the number of bound vortices m, which determines the spacing between bound vortices. The first candidate for the time increment, Δt_d, depends on the heave motion and is determined by m and the stroke line length d such that the distance covered by the heave motion in a time increment is equal to the spacing between the bound vortices. Another candidate, Δt_p, is determined by the pitch speed p (see Appendix B) such that the pitch event is fully contained within the time increment. The smaller of the two is used for the actual time increment. Notice that m is the only non-physical parameter that can be selected independently from all other physical parameters, including d and p, that define the problem. Denda et al. (2016) compared the solution with results obtained by a Navier–Stokes solver, OpenFOAM (Weller, Tabor, Jasak, & Fureby, 1998), based on the FVM. Second, the closeness between the vortex source and the observation is explored when we evaluate the velocity. Obviously, the velocity increases as we get closer to a vortex. The strategy to avoid this type of singularity is employed by introducing the vortex core model or Rankine vortex.

Next, the numerical performance for the single-wing case is summarised. As m is increased, the solution has improved rapidly for $m = 3, 5, 10, 15, 20$. The solution stabilised and approached towards the OpenFOAM solution around $m = 20, 25, 30, 35$ but began to deviate from the OpenFOAM solution after $m = 35$. The solution does not seem to converge to the viscous solution as we increase m. For a large m, the wake is packed with vortices and, unless special techniques such as lumping nearby vortices or allowing vortex decay, numerical difficulties are expected even with the use of vortex core model designed to avoid this problem. For $m = 35$, the vortex method is approximately 20 times faster than the OpenFOAM. Rather than attempting to achieve the convergence to the reference solution obtained by the Navier–Stokes solver, it would be wise to know the limit of the present method and use it in the range that gives the optimal results. Our surprising discovery is that, although the results using a small m are quantitatively inferior, they still preserve the essence of the solution qualitatively. For a smaller $m(<35)$, the vortex method is significantly more than 20 times faster than the OpenFOAM. We have found that for $m>35$, the computational time increases exponentially but the numerical results deteriorate as compared to the OpenFOAM solution. The optimal value of m, determined by the accuracy and the computation time, is therefore around 35. The above observation gives us the best use of the proposed method as a quick solver for unsteady flapping problems. Using a small m, such as $m=5$ and $m=10$, we can explore the unknown unsteady behaviour of the flapping flight. Once we discover an interesting phenomenon or behaviour, we can increase m (up to $m=35$) for more accurate results. If the phenomenon needs to be further scrutinised, then we switch to a Navier–Stokes solver. We can remain confident that using this method with a small m both captures the essential behaviour and yields quick calculations.

We assume that the characteristics of the vortex method discovered for the single-wing case remain true for the two-wing case considered here. This assumption is quite safe since, in the transition from the single-wing to two-wing case, no new elements in the numerical algorithm are introduced. To complete the evaluation of numerical performance, we have performed a convergence study for the two-wing problem which is specified by Table 1. The case of synchronous flapping (zero phase shit) was considered. Figures 7 and 8 show the variation of the lift force F_y and the drag force F_x over one period from the start for various values of m. Up until $m=20$, the value of the forces jumped quickly until the variation slowed down after $m=20$ to show the sign of convergence towards $m=35$. The situation is very similar to the case of single-wing and we expect the solution begins to diverge after $m=35$, indicating the optimum value of m is between $m=20$ and $m=35$. Comparison of the vortex method solutions with those by the Navier–Stokes solver for the two-wing problem is in preparation.

Table 1. Flight parameters for the dragonfly, common to fore and hind-wings.

Translational velocity	$U=100\text{cm/s}$, $V=0\text{cm/s}$
Wing half-span and chord lengths	$l=5\text{cm}$, $c=0.8\text{cm}$
Distance of the stroke line from the body mass centre	$b=1.0\text{cm}$
Top and bottom stroke angles	$\phi_T=45^\circ$, $\phi_B=-45^\circ$
Stroke line angle	30°
Flapping frequency	$f=30\text{Hz}$
Pitching speed, amplitude, offset	$p=5$, $\gamma_m=30^\circ$, $\mu=0$
Pitch axis offset	$a=0\text{cm}$

The body axis angle $\delta=0^\circ$. See Figures 1 and 2.

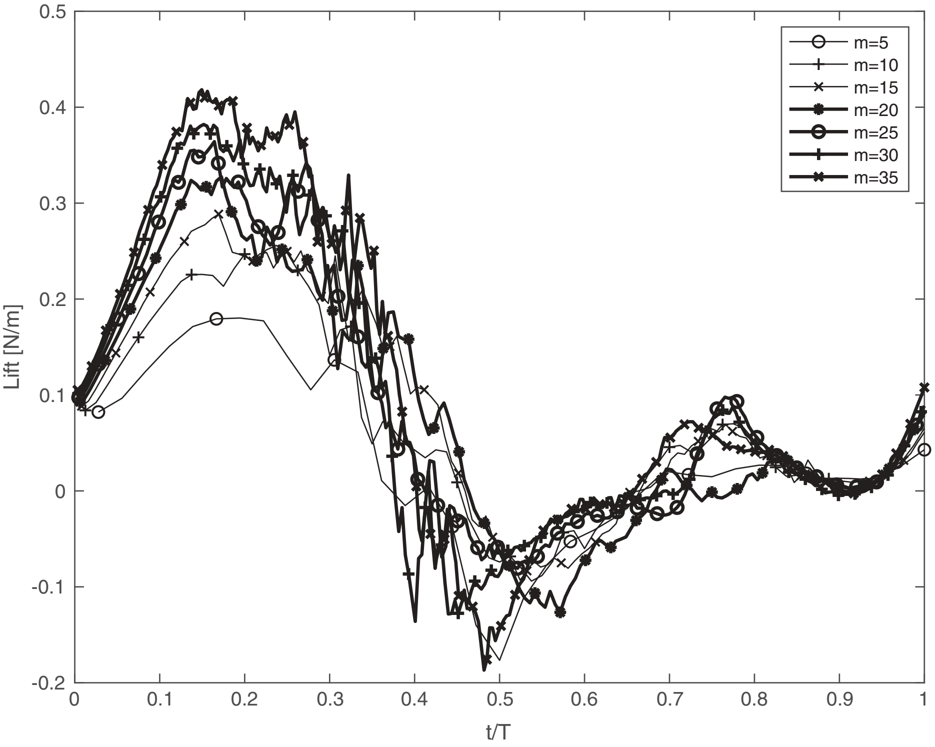

Figure 7. Variation of the lift force F_y over one period for various values of m.

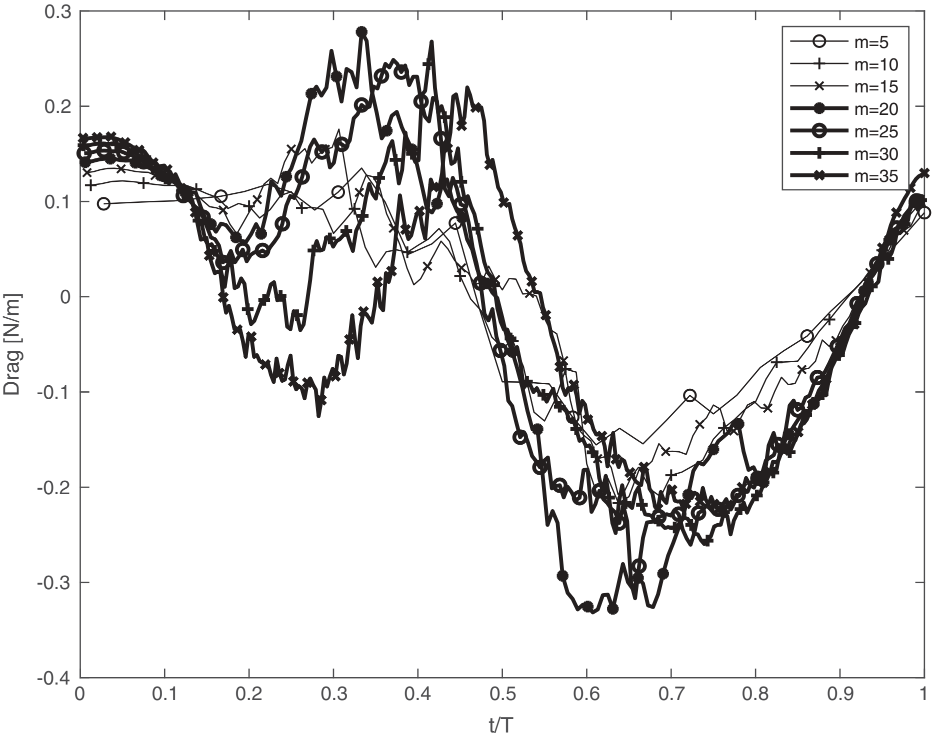

Figure 8. Variation of the drag force F_x over one period for various values of m.

10. Preliminary study on the role of the second pair of wings in insect flight

According to Wigglesworth (1972), in Hymenoptera (bee, wasp), Tricoptera (caddisfly), Lepidoptera (butterfly, moth) and Hemiptera (true bugs), 'fore and hind-wings are united by various mechanisms to make a functional unit' to avoid 'the disadvantage of the second pair of wings working in a region of turbulence produced by the first pair'. In Orthoptera (grasshopper, cricket, katydid and locust), Neuroptera (lacewing, mantidfly and antlion), Isoptera (termite) and Odonata (dragonfly and damselfly), the fore and hind-wings move independently. Wigglesworth compares the flight of Orthoptera and lower Neuroptera to that of Odonata (dragonflies). While the upstroke and downstroke of the fore-wings for the former group of insects are in advance of the hind-wings, the dragonflies reverse the order of the wing beat to avoid the difficulty.

Notice that the order of the hind-wing and the fore-wing beating is relative in the cyclic beating situation and there is no absolute way to specify which beats first. Rather, this issue should be addressed in terms of the phase shift of the hind-wing beating relative to the fore-wing, which ranges from 0° to 360°. Therefore, we first investigate the effects of the phase shift in the two-wing flapping. The geometric (wing chord, wing length, fore and hind-wing separation distance), kinematic (stroke plane angle, stroke angles, pitch shift) and kinetic parameters (flapping frequency, flight speed, pitch rate) are determined from a sample dragonfly species and its high-speed flight video as listed in Table 1; the exact identification of the dragonfly is not important in this study since we are not investigating dragonfly flight itself.

10.1. The effects of phase shift

Using the parameters in Table 1 taken from a typical dragonfly, we have performed flight analysis by varying the phase shift of the hind-wing relative to the fore-wing. The initial position of the fore-wing is at its maximum upper stroke angle ($\phi_T = 45^\circ$). The initial position of the hind-wing is shifted at various angles, relative to the fore-wing, ranging from 0° (synchronised) all the way up to 360°. Notice that at 360°, we return to the initial synchronised case of 0° phase shift. Figure 9 shows the average lift force over a flapping cycle as the function of the phase shift. It also shows the standard deviation of the lift force over the same cycle. The number of the bound vortices used in all the cases in this paper is $m = 10$. The results have been confirmed by calculations using $m = 15$.

Notice that the average lift force peaks at around 110° phase shift but remains near the peak level for phase shift angle between 0° and 180°. For the

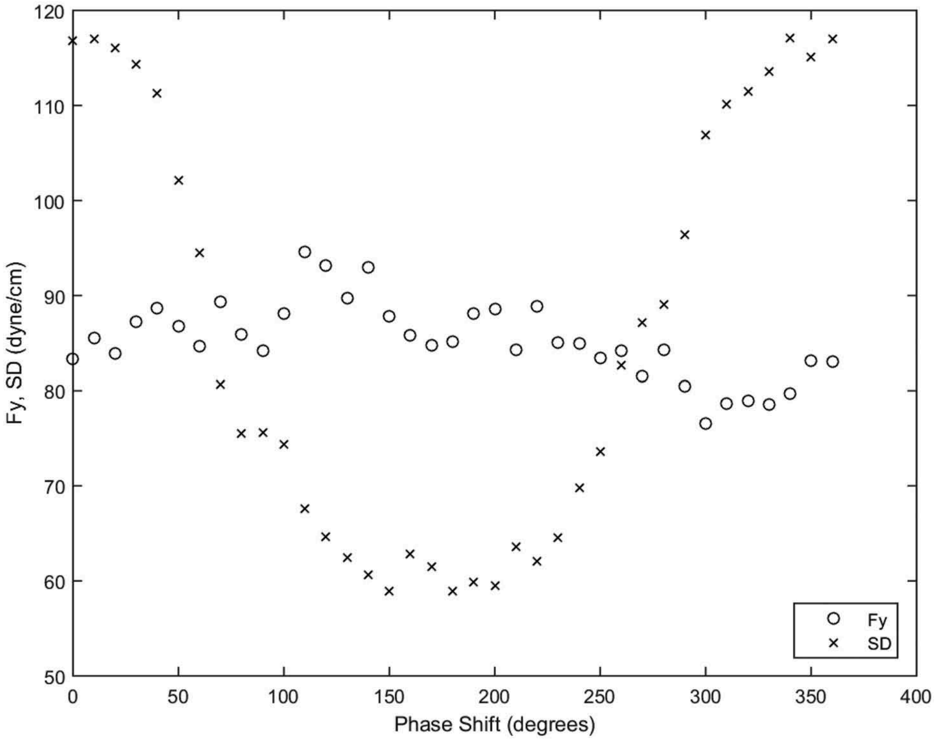

Figure 9. The average lift force F_y and the standard deviation (SD) over the cycle as the function of the phase shift.

phase shift larger than 180°, the lift force drops a little with the minimum lift force at around 300°. While the average lift force remains practically constant for all the phase shift angles, the standard deviation over the cycle varies drastically. The standard deviation takes the maximum value at 0° (and near 360°) phase shift and minimum at about 180° phase shift. The standard deviation indicates the stability of the flight; the smaller the standard deviation, the stabler the flight. Therefore, taking into account the relatively constant average lift force over the cycle, the 180° phase shit, with its minimum standard deviation, provides the most stable flight.

10.2. Power versus stability in insect flight

Based on the results of the study of the phase shift effects obtained above, we are singling out two cases: one is the synchronous flapping (phase shift 0°) and another is the asynchronous flapping (phase shift 180°) of the two-wing problem. We now investigate the variation of the lift force over the flapping cycle for each case.

Figure 10 shows the variation of the lift force for the synchronous flapping. In contrast, Figure 11 shows the lift force variation for the asynchronous flapping.

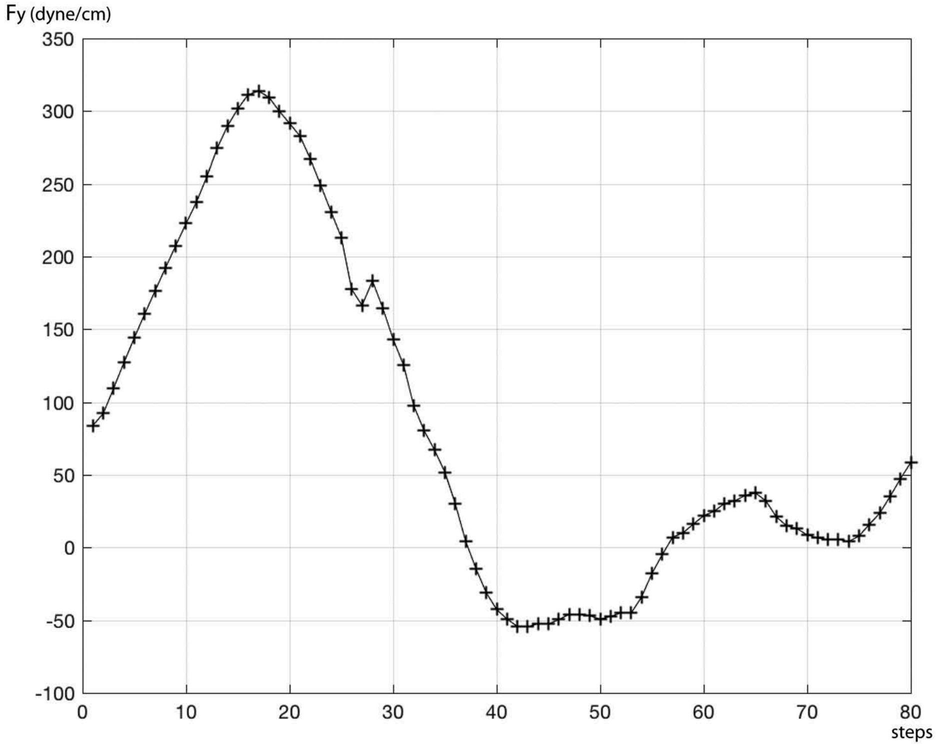

Figure 10. Lift force variation for the synchronous flapping.

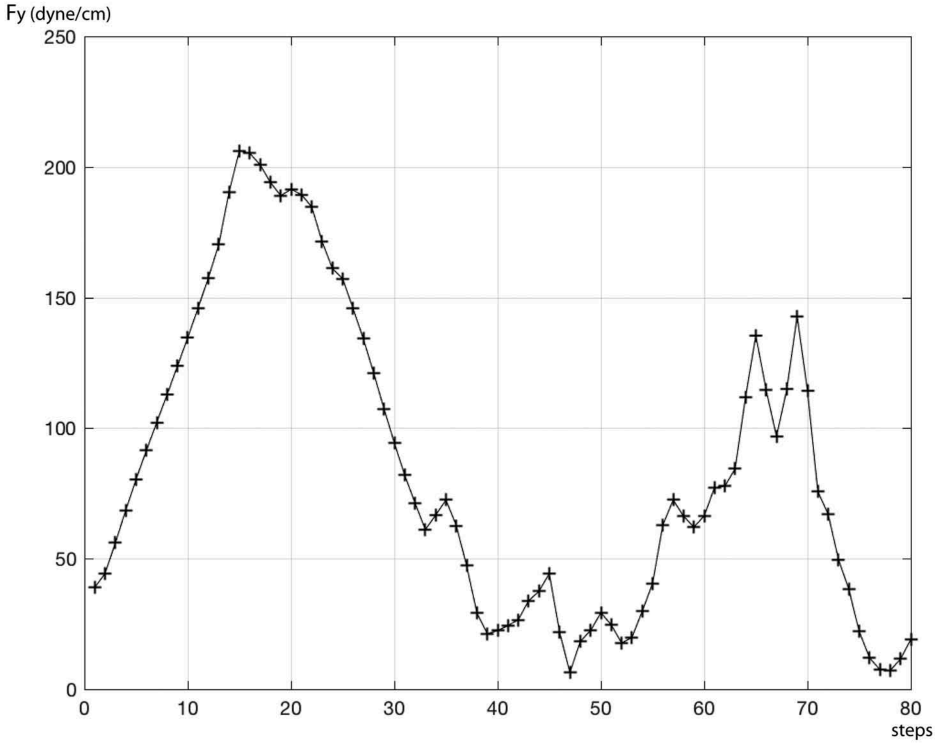

Figure 11. Lift force variation for the asynchronous flapping (phase shift 180).

Although the average lift force over the cycle may be comparable for the asynchronous and synchronous flapping cases, their variations over the cycle are drastically different. The value of the lift force for the asynchronous flapping remains positive throughout the cycle. In comparison, the synchronous flapping provides larger lift force than the asynchronous case in the downstroke; however, it suffers the severe loss of the lift force in the upstroke. Figure 12 shows the wake vortex distribution for the synchronous flapping at a moment of low lift force generation (step 50 in Figure 10). The corresponding velocity field is shown in Figure 13. Figure 14 shows the wake vortex distribution at a low lift generation (step 60 in Figure 11) for the asynchronous flapping. The corresponding velocity field is given by Figure 15. The comparison of the wake vortex distribution plot and the velocity field plot demonstrates the difference of the two presentations. In the wake vortex distribution plot, we can identify the pressure distribution in the air by looking at the population of the vortices around the wings. According to the Bernoulli equation, the pressure is low where the velocity is high. Therefore, if one side of a wing is populated by vortices and the other side is not, the pressure on the side with more vortices is lower than the other side and the force acts on the wing from the high-pressure to low-pressure side. By looking at the wake vortex distribution plot, we can visualise the force acting on the wings. Meanwhile, the velocity field plot does not provide the insight on the force acting on the wings but can be used to compare the results obtained with other methods.

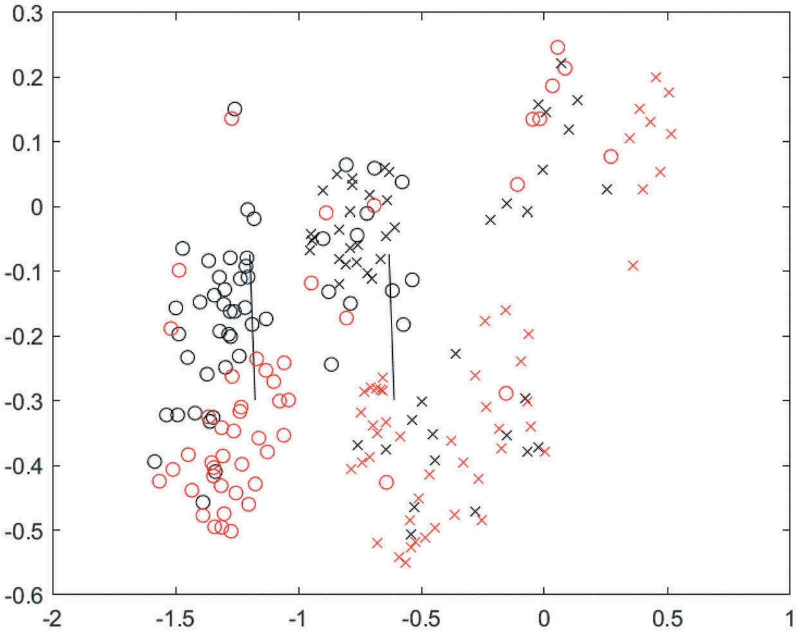

Figure 12. Wake vortex distribution for the synchronous flapping at a low lift generation step. The circle and cross represent vortices from the fore and hind-wings, respectively.

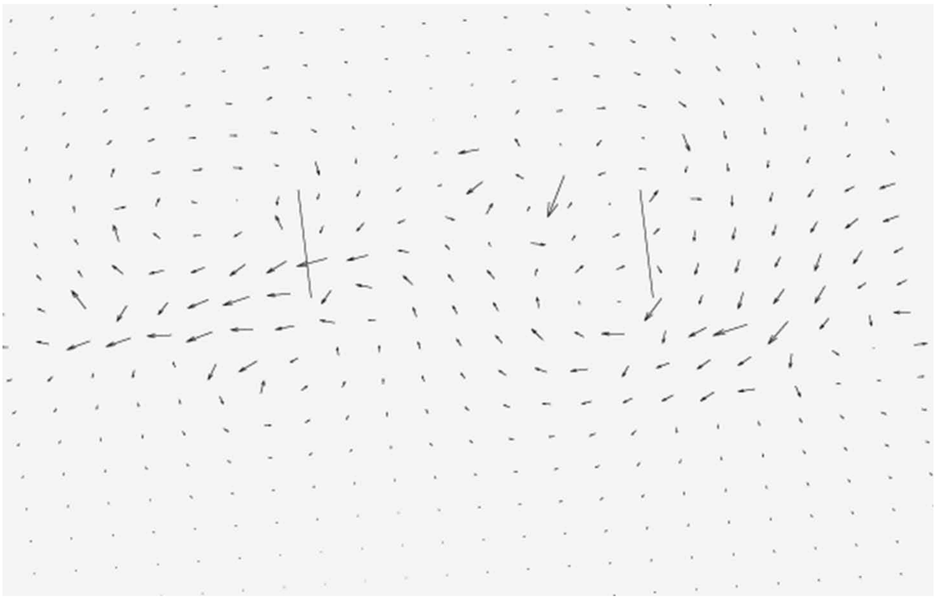

Figure 13. Velocity distribution for the synchronous flapping at a low lift generation step corresponding to the wake vortex distribution of Figure 12.

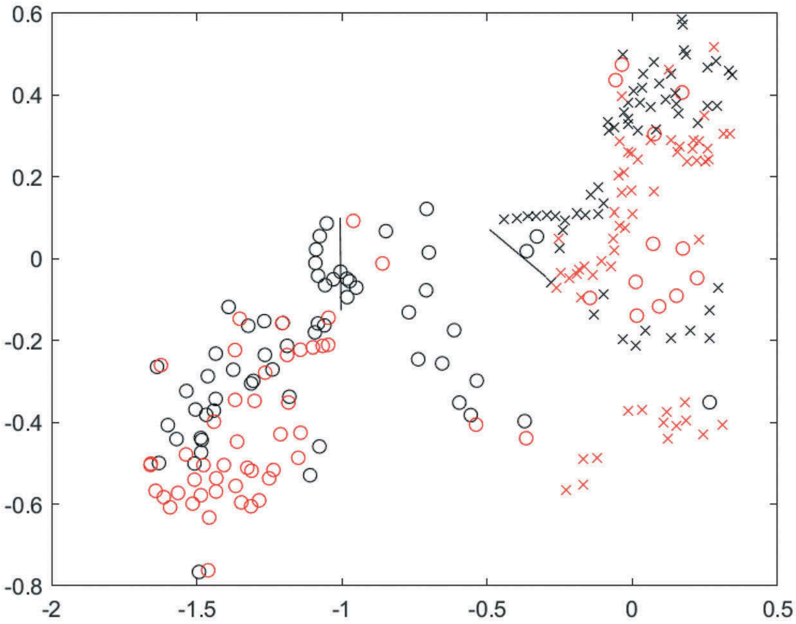

Figure 14. Wake vortex distribution for the asynchronous flapping at a low lift generation step. The circle and cross represent vortices from the fore and hind-wings, respectively.

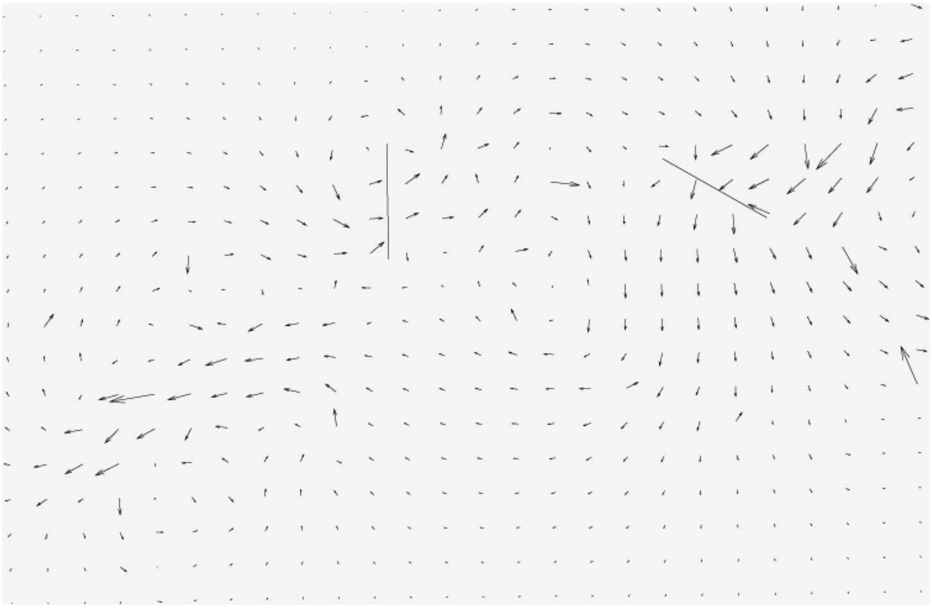

Figure 15. Velocity distribution for the asynchronous flapping at a low lift generation step corresponding to the wake vortex distribution of Figure 14.

Notice that for the synchronous flapping, the hind-wing is in the middle of the cloud of wake vortices, resulting in low negative lift force. In comparison, the hind-wing for the asynchronous flapping stays away from the wake vortices generated by the fore-wing, avoiding the severe loss of lift force. Overall, the asynchronous flapping provides the stable flight at the loss of the lift, while the synchronous flapping provides more instant power at the expense of the stability of the flight. Image sequences of the wake development for the two cases for the entire cycle of one period are provided by Movie 1 (synchronous) and Movie 2 (asynchronous).

We have also provided three high-speed movies of dragonfly flight. During the regular flight, dragonflies fly using asynchronous flapping to achieve the stable level flight as shown in Movie 3. They also use the asynchronous flapping during the natural takeoff as shown in Movie 4, but when threatened they flap wings synchronously to gain the power to escape quickly as shown in Movie 5.

YouTube links for the movies are provided below

Movie 1 https://youtu.be/oXsq1sUou74
Movie 2 https://youtu.be/OEWHxwPBHm8
Movie 3 https://youtu.be/pGpsvsDdqUg
Movie 4 https://youtu.be/qDZzLwfUExg
Movie 5 https://youtu.be/8a7MfqqFPmc

10.3. Two-wing versus united single-wing flight

The following final analysis is motivated by a feeble flight of Neuroptera (lacewing, mantidfly and antlion) whose hing-wings experience the difficulty in comparison to dragonflies. In the context of our phase shift analysis, the phase shift of the dragonflies is at around 180°, while that of the Neuroptera is around 0°, which is synchronous flapping. Indeed, the Neuroptera species flap their wings synchronously resulting in feeble and vertically oscillating flight. This is explained by our earlier results for the synchronous flapping. But what happens if the two wings (or two pairs of 3D wings) are combined into a larger single wing (one pair of 3D wings)? Does the combined larger wing yield improved performance?

The first analysis has been performed using the two-wing programme with the synchronous flapping as introduced earlier, in which the effects of the separation distance between the two wings are observed. The parameters used are the same as before, except the separation distance, which is defined as the sum $b_S = b_F + b_H$ of the separation distances of the fore and hind-wings measured from the mass centre $\hat{C}$ as shown in Figure 2. At a large separation distance, the two wings flap independently without interaction; the lift calculated is 290 dyn/cm, which remains constant as separation increases. As b_S is decreased, the wings begin to interact and the lift force increases up to a peak value of 320 dyn/cm . Then, the lift force suddenly drops to 260 dyn/cm as two wings get extremely close. Notice that the dropped value is smaller than the lift force achieved by a large separation, indicating the destructive interaction of the wings. This is in contrast to the constructive interaction observed at a moderate separation distance, in which the lift force is greater than the force generated by a large separation. In the second analysis for the single wing, all parameters are kept the same as the two-wing case except the chord length is doubled, indicating the unity or linking of the two wings. The maximum lift force in the downstroke is 225 dyn/cm, as shown in Figure 16. In all the cases considered, the maximum lift force is observed during the downstroke, at about the same time in the flapping cycle. The shape of the lift force curves remains almost identical for both the two-wing and the single-wing cases.

Although we have been expecting the combined single-wing to produce more lift force than the two-wing synchronous flapping, it is not the case. This means that the two wings flapping independently but synchronously will produce more lift force than the single wing with the same surface area as the two wings combined. Additionally, if the separation distance is properly adjusted, then the synchronous two-wing flapping can achieve the constructive interaction between the two wings to maximise the lift force. Finally, whether wings are united or remain separated, as long as the wings move synchronously, stability is lost and insects cannot achieve the level flight.

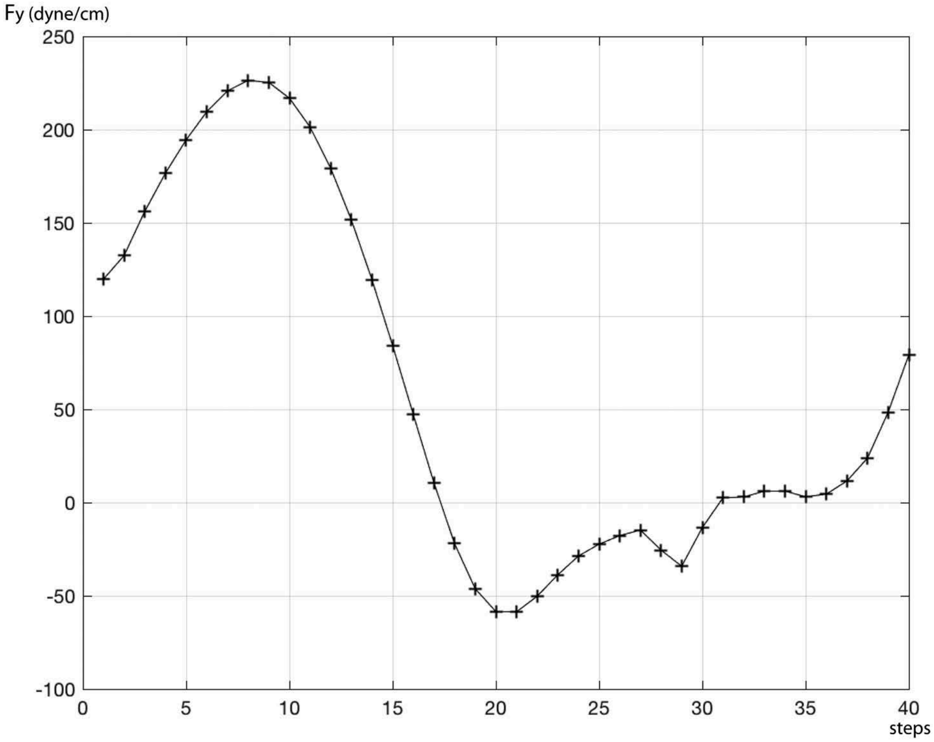

Figure 16. Lift force variation for the united fore and hind-wing flapping.

11. Concluding remarks

We have developed a simple but efficient numerical technique for the analysis of the flapping with two pairs of wings in 2D using the vortex method. Using this technique, we have performed a preliminary study on the effects of two pairs of wings in insect flapping flight.

Dragonflies manage to adopt two strategies in their flight. Regularly, they use the asynchronous flapping for stability, but occasionally they adopt the synchronous flapping for power. They can do this because they keep the two pairs of wings separated. The majority of the other insects unite their fore and hind-wings to provide more lift force in the downstroke. However, flapping two pairs of wings synchronously seems to produce more lift force than flapping with one pair of larger wings obtained by combining the two.

Disclosure statement

No potential conflict of interest was reported by the authors.

ORCID

Mitsunori Denda http://orcid.org/0000-0001-9652-3540

References

Azuma, A., & Watanabe, T. (1988). Flight performance of a dragonfl. *The Journal of Experimental Biology*, *137*, 221–252.

Belotserkovsky, S. M., Kotovskii, V., Nisht, M., & Fedorov, R. (1993). *Two-dimensional separated flows*. Boca Raton: CRC Press.

Belotserkovsky, S. M., & Lifanov, I. K. (2003). *Methods of discrete vortices*. Boca Raton: CRC Press.

Denda, M., Jujjavarapu, P. K., & Jones, B. C. (2016). A vortex approach to unsteady insect flight analysis in 2D. *European Journal of Computational Mechanics*, *25*(1–2), 218–247.

Rival, D. F., Widmann, A., & Tropea, C. (2012). A discussion on vortex growth and saturation in dragonfly-inspired flight. In T. Cameron & H. Bleckmanan (Eds.), *Nature inspired fluid mechanics* (pp. 149–158). Heidelberg: Springer.

Sears, W. R. (2011). *Introduction to theoretical aerodynamics and hydrodynamics*. Reston: AIAA.

Thomas, A. L. R., Taylor, G. K., Srygley, R. B., Nudds, R. L., & Bomphery, R. J. (2004). Dragonfly flight: Free-flight and tethered flow visualizations reveal a diverse array of unsteady lift-generating mechanisms, controlled primarily via angle of attack. *The Journal of Experimental Biology*, *207*, 4299–4323.

Wang, J. K., & Sun, M. (2005). A computational study of the aerodynamics and forewing–Hindwing interaction of a model dragonfly in forward flight. *The Journal of Experimental Biology*, *208*, 3785–3804.

Wang, Z. J., & Russell, D. (2007). Effect of forewing and hindwing interactions on aerodynamic forces and power in hovering dragonfly flight. *Physical Review Letters*, *99*, 148101.

Weller, H. G., Tabor, G., Jasak, H., & Fureby, C. (1998). A tensorial approach to computational continuum mechanics using object-oriented techniques. *Computers in Physics*, *12*(6), 620–631.

Wigglesworth, V. B. (1972). *The principles of insect physiology* (7th ed.). London: Chapman and Hall.

Appendices

Appendix A. Key coordinates in space-fixed system

The coordinates used in the description of the wing motion are all given in the space-fixed system. The following formulas are applicable to both fore and hind-wings with additional subscripts F and H, respectively. See Figures 1 and 2.

$\hat{C}$: **mass centre of the body**

$$\tilde{\xi}_{\hat{C}} = -Ut, \tag{A.1}$$

$$\tilde{\eta}_{\hat{C}} = -Vt,$$

where U and V are constant velocity components of the air.

$\hat{B}$: **intersection of stroke line and body axis**

$$\tilde{\xi}_{\hat{B}} = \tilde{\xi}_{\hat{C}} + b\,\cos(\delta), \tag{A.2}$$

$$\tilde{\eta}_{\hat{B}} = \tilde{\eta}_{\hat{C}} - b\,\sin(\delta),$$

where b is the body-axis coordinate of the attachment point, B, of the stroke plane measured from the body centre, $\hat{C}$, and δ is the angle of the body-axis.

$\hat{O}$: **origin of the wing-translating system**

$$\tilde{\xi}_{\hat{O}} = \tilde{\xi}_{\hat{B}} + D\,\cos(\beta-\delta) = -Ut + b\,\cos(\delta) + D\,\cos(\beta-\delta), \tag{A.3}$$

$$\tilde{\eta}_{\hat{O}} = \tilde{\eta}_{\hat{B}} + D\,\sin(\beta-\delta) = -Vt - b\,\sin(\delta) + D\,\sin(\beta-\delta),$$

where β is the angle of the stroke line with respect to the body axis and D is defined by Equation (A.8).

O: **origin of the wing-fixed system**

$$\tilde{\xi}_{O} = \tilde{\xi}_{\hat{O}} + a\cos(\alpha), \tag{A.4}$$

$$\tilde{\eta}_{O} = \tilde{\eta}_{\hat{O}} - a\sin(\alpha),$$

where a is the distance of the origins of the wing-translating, $\hat{O}$, and wing-fixed, O, systems and α is the attack angle of the wing.

P: **a point on the wing**

$$\tilde{\xi}_{O} = \tilde{\xi}_{\hat{O}} + (a+\xi)\cos(\alpha), \tag{A.5}$$

$$\tilde{\eta}_{O} = \tilde{\eta}_{\hat{O}} - (a+\xi)\sin(\alpha),$$

where $(\xi,\,0)$ is the coordinates of the point P in the wing-fixed system.

Appendix B. Wing motion

B1. *Lunge and heave*

In the following equations, the subscripts F and H, indicating the fore and hind-wing, are omitted. For each wing, we obtain the hypothetical wing length l (half the actual wing length $\mathcal{L} = 2l$) and top and bottom stroke angles (ϕ_T and ϕ_B) from the insect specimen considered. The stroke line length is given by

$$d = d_T + d_B, \tag{A.6}$$

where $d_T = l\sin(\phi_T)$ and $d_B = l\sin(-\phi_B)$. The minus sign is required since the default sign for ϕ_B is negative. As shown in Figure 1, the origin $\hat{O}$ of the wing-translating system, located on the stroke line and moving along it, has its global position given by $(L - Ut, H - Vt)$, in terms of the heave H and lunge L and the ambient air velocity components, U and V, where

$$L = b\,\cos(\delta) + D\,\cos(\beta - \delta), \tag{A.7}$$

$$H = -b\,\sin(\delta) + D\,\sin(\beta - \delta),$$

obtained from Equation (A.3) with

$$D = \frac{1}{2}\left(d\,\cos\frac{2\pi(t+\tau)}{T} + e\right), \tag{A.8}$$

where $e = d_T - d_B$ is the stroke length difference parameter between the top and bottom strokes, τ and T are the phase shift and the period of motion and β is the stroke line angle. The rates of lunge and heave are obtained by the time derivatives

$$\dot{L} = -\frac{\pi d}{T}\sin\frac{2\pi(t+\tau)}{T}\cos(\beta - \delta), \tag{A.9}$$

$$\dot{H} = -\frac{\pi d}{T}\sin\frac{2\pi(t+\tau)}{T}\sin(\beta - \delta). \tag{A.10}$$

B2. *Pitch (Rotation)*

As shown in Figure 1, the rotation (pitch) γ (positive clockwise) of the wing occurs about the origin $\hat{O}$ of the wing-translating system. With a non-zero pitch, the attack angle of the chord line is given by $\alpha = \pi/2 - (\beta - \delta - \gamma)$. If the pitch occurs exactly at the top or bottom of the stroke, then it is called symmetrical pitch. The timing of the pitch can be either exactly at the top and bottom of the stroke (symmetric), before them (advanced pitch) or after (delayed pitch), which is specified by an timing offset parameter μ ($\mu < 0$ for advanced and $\mu > 0$ for delayed pitch).

Actual insects can never achieve the sudden pitch (Figure 4) and the pitch motion is smoothed significantly. This smoothed pitch motion is described by the function

$$f_{t_i} = \frac{2}{1 + e^{-2p(t-t_i)}}, \tag{A.11}$$

which describes the step function (jump from 0 to 1 at $t = t_i$) when $p \to \infty$. The magnitudes of the supination and pronation are given by $+2\gamma_m$ and $-2\gamma_m$, respectively. The entire series of smooth pitching in one period is given by the superposed smooth step functions,

$$\gamma = \gamma_m(1 - f_0 + f_{T/2} - f_T). \tag{A.12}$$

Figure 5 shows variations of smooth pitching with symmetric, advanced and delayed pitching.

The pitch rate is given by

$$\dot{\gamma} = \gamma_m(-\dot{f}_0 + \dot{f}_{T/2} - \dot{f}_T), \tag{A.13}$$

where

$$\dot{f}_{t_i} = \frac{4pe^{-2p(t-t_i)}}{\left(1 + e^{-2p(t-t_i)}\right)^2}. \tag{A.14}$$

The parameter p controls the speed of pitch. Let Δt_p be the time the smoothed step function f_{t_i} takes to complete the smooth increase of pitch by the amount $2\gamma_m$. It is shown by Denda et al. (2016) that p is given by

$$p = \frac{4}{\Delta t_p}. \tag{A.15}$$